

Superconducting solenoid optimization and fields measurement

S. Ma,^{1,*} A. Arnold,² P. Michel,² P. Murcek,² A. Ryzhov,² J. Schaber,² J. Teichert,^{2,†} and R. Xiang²

¹National Key Laboratory of Science and Technology on Advanced Laser and High Power Microwave,
Institute of Applied Electronics, China Academy of Engineering Physics, Mianyang 621900, China.

²Helmholtz-Zentrum Dresden-Rossendorf, 01328 Dresden, Germany

To compensate the projected transverse beam emittance, a solenoid is typically used in normal-conducting and superconducting radio frequency (SRF) photoinjectors. In the ELBE SRF Gun-II, a superconducting solenoid is positioned inside the gun's cryomodule, approximately 0.7 m from the end of the gun cavity. The spherical aberration and multipole fields effects, caused by offset and tilt, limit the reduction of beam emittance for high bunch charge. We have designed a new superconducting (SC) solenoid with a lower spherical aberration coefficient. From the simulation, beam emittance from spherical aberration decreases by 47%. Both the longitudinal and transverse fields are measured and analyzed using the formalism fitting method to assess the SC solenoid's performance within the cryomodule and its influence on beam transverse emittance.

Keywords: Superconducting solenoid, magnetic field, photoinjector, SRF Gun.

I. INTRODUCTION

A superconducting radiofrequency (SRF) electron source has demonstrated the capability to produce high-quality electron beams over the past decade, specifically for the "Electron Linac for Beams with High Brilliance and Low Emittance (ELBE)," a user facility that generates secondary radiation for a wide range of applications [1–3]. The SRF gun, primarily operating in continuous wave (CW) mode at repetition rates of 50 kHz and 100 kHz, has been instrumental in producing terahertz radiation between 0.2 and 1.5 THz, characterized by high pulse energy and significant average power. Equipped with a 3.5-cell niobium cavity resonating at 1.3 GHz, the SRF gun achieves an acceleration gradient of 8 megavolts per meter (MV/m), corresponding to an on-axis peak electric field of 20.5 MV/m. The SRF gun is capable of delivering electron bunches with up to 300 pC bunch charge, utilizing either magnesium (Mg) or cesium telluride (Cs₂Te) cathodes in conjunction with a 262 nm laser [4–10]. This technology shows great promise for applications in neutron time-of-flight experiments, high-repetition-rate ultrafast electron diffraction (UED), high-power terahertz experiments, and Thomson backscattering experiments that require high bunch charge and high repetition rates [11–14].

To control the electron beam size and compensate for projected transverse emittance, a superconducting (SC) solenoid is installed 0.7 meters downstream from the cavity's end within the SRF gun cryomodule [15, 16]. This distance represents a balanced compromise between the need for magnetic field shielding of the cavity and the minimization of beam emittance. However, a solenoid will introduce a new source of emittance due to the spherical aberration, which is linear with respect to the spherical aberration coefficient and scales with the fourth power of beam RMS size [17]. For beams with relatively large diameters, the solenoid's spherical aberrations can significantly increase emittance [18]. Ad-

ditionally, measurements indicate that beam aberrations increase with higher solenoid currents, primarily due to multipole magnetic fields effect arising from tilt and offset position errors of the solenoid [19, 20]. This configuration imposes limitations on applications such as X-ray free-electron laser (XFEL) facilities, which demand lower emittance and higher bunch charge [21–23].

The current SRF gun in operation at ELBE (SRF Gun-II) is part of a developmental progression in SRF gun research and development, which will soon advance to the third-generation SRF Gun-III [24, 25]. The primary objectives for this new generation are to increase the available bunch charge for terahertz production and to reduce transverse emittance through enhanced emittance compensation, correction of multipole magnetic fields effect, and mitigation of solenoid aberrations. To achieve these goals, a newly redesigned solenoid has been constructed. With the completion of the SRF Gun-III cryomodule, we have conducted magnetic field measurements to evaluate the new solenoid's performance. A formalism fitting method was employed to analyze the multipole fields, and the associated measurement errors were quantified. We also assessed the impact of these fields on beam emittance. In this paper, the first part is the basic concept and field measurement methods. The influence of the multipole components, such as the quadrupole and sextupole, is analyzed in this part. The comparison of new and old design SC solenoids is given in the second part. The third part presents the results of the filed and error analyses. The fourth part analyzes the multipole fields' influence on beam transverse emittance and the solutions. The conclusion is given in the last part.

II. BASIC PRINCIPLE

A. The spherical aberration of solenoid

Magnetic lenses can exhibit imaging errors even when the momentum distribution of the particles is negligibly small. These errors arise due to spherical aberrations, which occur as a result of nonlinear magnetic field regions within the lens and from particle rays that deviate from the paraxial approxima-

* Corresponding author: ms369@mail.ustc.edu.cn.

† Corresponding author: j.teichert@hzdr.de.

tion. Spherical aberration exhibits a dependence on the third power of the particle's radial position within the solenoid and can be represented through two distinct integral expressions [17]:

$$C_S = \frac{1}{2} \frac{\int B(z)^2 dz}{\int B(z)^2 dz}. \quad (1)$$

The transverse emittance resulting from solenoid spherical aberration can be calculated as:

$$\varepsilon_{sph} = \frac{r_0^4}{2\sqrt{6}f} \sqrt{\frac{C_1^2}{12} + \frac{C_1 C_2}{5} r_0^2 + \frac{C_2^2}{8} r_0^4}, \quad (2)$$

$$\begin{aligned} C_1 &= C_s \\ C_2 &= \frac{5}{64} \frac{\int B(z)''^2 dz}{\int B(z)^2 dz}. \end{aligned} \quad (3)$$

On the right side of Eq. 2, the higher-order terms are significantly smaller than the leading term. Thus, the spherical aberration emittance scales with the fourth power of the beam RMS size at the solenoid entrance. In high bunch charge and short bunch length injectors, the beam RMS size is typically large, which amplifies the impact of spherical aberration. Therefore, it is crucial to decrease the spherical aberration coefficient to mitigate its effect on beam quality. As indicated by Eq. 1, reducing the spherical aberration coefficient requires minimizing the integral of the first derivative of the solenoid field at the same field integral.

B. The solenoid axis and multipole fields measurement

Pulsed wire method is a basic method to analyze the alignment of magnets [26]. In this method, a wire is fixed between two points though the external field. A current pulse is applied to the wire. If the external field has transverse component, the local wire will give a motion due to Lorentz force, which will propagate to two endpoints as traveling wave and measured by motion sensors. The amplitude of motions is related to the transverse magnetic field integration along the z direction and the pulse current magnitude. The external field's axis can be obtained within 100 μm resolution from analysis of the motions. For solenoids, the other method is to use the properties of solenoid's field that the longitudinal component on the axis is the extremum along the radial direction and the radial component is zero, shown as:

$$\begin{aligned} \frac{\partial B_z(r, z)}{\partial r} &= 0 \\ B_r(0, z) &= 0. \end{aligned} \quad (4)$$

This method has worse resolution than the pulsed wire, but is concise for the superconducting solenoid. Because only one end face of tube is open in the cryomodule and difficult to construct the wire.

For multipole components measurement, an important method to analyze the multipole magnetic field is the harmonic coils and wires, which developed by Carlo et al. at CERN LHC [27, 28]. The basic idea relies on Faraday's law of induction: as the magnetic field changes, it induces an electromotive force (EMF) in the coils, enabling the accurate determination of the multipole field components. The Fourier coefficients of the magnetic flux function correspond to the strength of the field's multipole components.

Although this method provides highly accurate measurements of fields, it necessitates a multifaceted control system and advanced electrical analysis tools. This approach is impractical for accelerator facilities without access to a dedicated field measurement laboratory. To streamline the measurement of multipole modes without the need for specialized equipment, we use a 2D polynomial fitting technique based on data obtained from a 3D Hall probe measurements. Drawing on the definitions of dipole, quadrupole, and sextupole components as outlined in [29], we proceed with the following approach:

$$\begin{aligned} \mathbf{B}_{dn} &= 0\mathbf{e}_x + J_{dn}\mathbf{e}_y \\ \mathbf{B}_{ds} &= -J_{ds}\mathbf{e}_x + 0\mathbf{e}_y \\ \mathbf{B}_{qn} &= J_{qn}y\mathbf{e}_x + J_{qn}x\mathbf{e}_y \\ \mathbf{B}_{qs} &= -J_{qs}x\mathbf{e}_x + J_{qs}y\mathbf{e}_y \\ \mathbf{B}_{sn} &= J_{sn}xy\mathbf{e}_x + \frac{1}{2}J_{sn}(x^2 - y^2)\mathbf{e}_y \\ \mathbf{B}_{ss} &= -\frac{1}{2}J_{ss}(x^2 - y^2)\mathbf{e}_x + J_{ss}xy\mathbf{e}_y, \end{aligned} \quad (5)$$

the field coefficients are represented by J . The subscripts 'd', 'q', 's' denote the dipole, quadrupole, sextupole part, respectively, while 'n' and 's' specify whether the mode is of the normal or skew type. In the case of solenoids, the transverse magnetic field can be expressed as:

$$\mathbf{B}_t = J_t x \mathbf{e}_x + J_t y \mathbf{e}_y. \quad (6)$$

So the horizontal and vertical fields can be presented as form:

$$\begin{aligned} B_x &= -J_{ds} + J_{qn}y + (J_t - J_{qs})x + \\ &\quad J_{sn}xy - \frac{1}{2}J_{ss}(x^2 - y^2) + \dots \\ B_y &= J_{dn} + J_{qn}x + (J_t + J_{qs})y + \\ &\quad \frac{1}{2}J_{sn}(x^2 - y^2) + J_{ss}xy + \dots \end{aligned} \quad (7)$$

The Hall-effect sensor can measure the horizontal and vertical components of the transverse magnetic field accurately. The coefficients for various multipole modes (e.g., quadrupole and sextupole) can then be derived by applying a numerical fitting algorithm to the functions provided in Eq. 7.

C. The influence of multipole fields on beam transverse emittance

The multipole fields resulting from misalignment and manufacturing errors in the solenoid can affect the beam shape

and emittance. Since the dipole field components primarily cause beam deflection, our focus will be on the effects of the quadrupole and sextupole components. Details on the influence of these fields and methods for their correction can be found in references [30].

The four-dimensional phase space transport matrix for an ideal quadrupole lens under the thin lens approximation followed by a solenoid lens can be expressed as follows:

$$M_{\text{sol}} M_{\text{quad}} = \begin{pmatrix} \cos^2 KL_s & \frac{\sin KL_s \cos KL_s}{K} & \sin KL_s \cos KL_s & \frac{\sin^2 KL_s}{K} \\ -K \sin KL_s \cos KL_s & \cos^2 KL_s & -K \sin^2 KL_s & \sin KL_s \cos KL_s \\ -\sin KL_s \cos KL_s & -\frac{\sin^2 KL_s}{K} & \cos^2 KL_s & \frac{\sin KL_s \cos KL_s}{K} \\ K \sin^2 KL_s & -\sin KL_s \cos KL_s & -K \sin KL_s \cos KL_s & \cos^2 KL_s \end{pmatrix} \begin{pmatrix} 1 & 0 & 0 & 0 \\ -\frac{1}{f} & 1 & 0 & 0 \\ 0 & 0 & 1 & 0 \\ 0 & 0 & +\frac{1}{f} & 1 \end{pmatrix}. \quad (8)$$

Here L_s represents the solenoid's effective length, defined as $\frac{\int B(z)^2 dz}{B_s^2}$, where $B(z)$ is the longitudinal magnetic field as a function of position z , and B_s is the peak magnetic field along the solenoid axis. The parameter $K = \frac{eB_0}{2mc\gamma\beta}$, e is the electron charge, m is the electron mass, c is the speed of light, γ is the relativistic factor, and $\beta = v/c$ is the normalized velocity of the particle.

A normal quadrupole lens, positioned at the entrance of the solenoid, provides focusing with a focal length f . After the beam passes through the normal quadrupole and solenoid, the resulting beam matrix takes the following form:

$$\sigma(s) = M_{\text{sol}} M_{\text{quad}} \sigma(0) (M_{\text{sol}} M_{\text{quad}})^T. \quad (9)$$

The additional transverse emittance, resulting from the combined effects of the quadrupole's focusing and the solenoid's coupling between transverse planes, is given by:

$$\varepsilon_{n, \text{quad} + \text{sol}} = \beta\gamma \frac{\sigma_{x, \text{sol}} \sigma_{y, \text{sol}}}{f} |\sin 2KL_s|. \quad (10)$$

If the quadrupole field has a rotating angle α_1 , the resulting transfer matrix incorporates cross-plane coupling terms between the x and y directions, and is given by:

$$M_{\text{rotquad}}(\alpha_1, f) = \begin{pmatrix} 1 & 0 & 0 & 0 \\ -\frac{\cos 2\alpha_1}{f} & 1 & -\frac{\sin 2\alpha_1}{f} & 0 \\ 0 & 0 & 1 & 0 \\ -\frac{\sin 2\alpha_1}{f} & 0 & \frac{\cos 2\alpha_1}{f} & 1 \end{pmatrix}, \quad (11)$$

and Eq. 10 changes to:

$$\varepsilon_{n, \text{quad} + \text{sol}} = \beta\gamma \frac{\sigma_{x, \text{sol}} \sigma_{y, \text{sol}}}{f} |\sin 2(KL_s + \alpha_1)|. \quad (12)$$

To mitigate the emittance growth caused by the quadrupole component parasiting the solenoid, a pair of correction quadrupoles, consisting of a normal quadrupole and a skew quadrupole, are installed downstream of the solenoid at a distance L . These quadrupoles work together and have a rotating angle α_2 ,

$$\varepsilon_{n, \text{total}} = \beta\gamma \left| \frac{\sigma_{x, \text{sol}} \sigma_{y, \text{sol}}}{f} \sin 2(KL_s + \alpha_1) + \frac{\sigma_{x, \text{cor}} \sigma_{y, \text{cor}}}{f_{\text{cor}}} \sin(2\alpha_2) \right|. \quad (13)$$

Eq. 13 demonstrates that the effectiveness of the corrector strongly depends on the beam's RMS size at the corrector's

position. In practical applications, the distance between the solenoid and the corrector is a key parameter. In the SRF gun configuration, the corrector is positioned 0.437 m downstream from the solenoid, just outside the cryomodule. Using ASTRA, a beam dynamics simulation tool [31], we performed simulations and compared the results to the theoretical predictions given by Eq. 12 and Eq. 13. Fig. 1 shows the results of simulations for different distances. The simulations reveal that, when the distance parameters are fixed, insufficient corrector focal strength will fail to properly counteract the quadrupole field from the solenoid. It indicates that for identical parasitic quadrupole strengths in both the solenoid and corrector, shorter distances result in more effective emittance compensation. However, if the distance is too large, as seen in the 0.7 m case (blue line) in Fig. 1, the corrector either fails to cancel the solenoid's quadrupole field or requires a significantly stronger focal strength to achieve the same effect.

According to Eq. 13, the beam size at the corrector is always smaller than at the solenoid, as the solenoid focuses the beam, and the corrector is positioned within the solenoid's focal length. Theoretically, if the corrector is placed beyond the solenoid's focal length, where the beam RMS size equals or exceeds that at the solenoid, the emittance compensation improves for a given quadrupole strength. However, because the solenoid's focal length varies depending on specific operational parameters, the corrector cannot compensate for emittance growth that occurs between the solenoid and the corrector. Therefore, for optimal emittance compensation, the corrector should be positioned as close to the solenoid as possible.

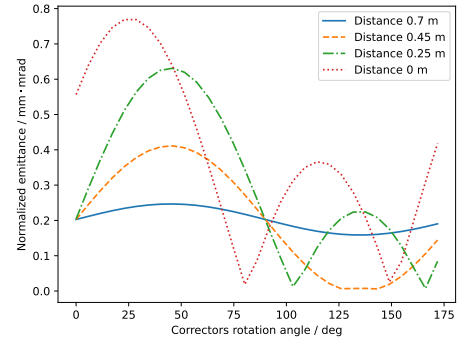


Fig. 1. Transverse beam emittance was evaluated using ASTRA simulations. The system comprises a quadrupole magnet integrated with a solenoid, where the quadrupole has an effective length of 0.04 meters, a strength of 0.5 m^{-2} , and is rotated by 23 degrees relative to the solenoid's principal axis. The beam has a kinetic energy of 4 MeV. The solenoid has a maximum magnetic field of 0.171 T, characterized by an effective length (L_s) of 0.04 meters. Additionally, a corrector magnet with an effective length of 62.7 mm and a focal length of 16 meters is positioned downstream to adjust the beam dynamics.

As discussed in references [32, 33], sextupole component can introduce additional transverse emittance to the beam which primarily dependent on the radial second-order derivative of the magnetic field, as well as the effective length of the

field region. To simplify the analysis of sextupole effects, we assume that fringe fields are negligible, a valid assumption in this context since fringe effects are minor compared to the main field. Additionally, we consider the paraxial approximation, where the beam's transverse momentum is much smaller than its longitudinal momentum. Under these conditions, the Lorentz force equation gives the force in the x-direction as:

$$F_x = \frac{dp_x}{dt} = e(v_y B_z - v_z B_y). \quad (14)$$

Considering that $dz = \beta c dt$, the force becomes:

$$\frac{dp_x}{dz} = -e B_y. \quad (15)$$

The y-component of the sextupole field is given by [29]:

$$B_y(x, y) = \frac{1}{2} \frac{\partial^2 B_y}{\partial x^2} \bigg|_{x,y=0} (x^2 - y^2). \quad (16)$$

The sextupole field introduces the transverse momentum as:

$$\begin{aligned} \int_{p_x}^{p_x + \Delta p_x} dp_x &= \Delta p_x = -\frac{e}{2} \int_{-\infty}^{\infty} \frac{\partial^2 B_y}{\partial x^2} \bigg|_{x,y=0} (x^2 - y^2) dz \\ \Delta p_x(x, y) &= -\frac{e}{2} \frac{\partial^2 B_y}{\partial x^2} \bigg|_{x,y=0} L_{eff} (x^2 - y^2). \end{aligned} \quad (17)$$

The beam emittance is

$$\varepsilon_n = \frac{\sigma_x \sigma_{p_x}}{mc}, \quad (18)$$

σ_x and σ_{p_x} are the RMS size and horizontal momentum of the beam, respectively:

$$\sigma_{p_x}^2 = \frac{\int_{-\infty}^{\infty} [\Delta p_x(x, y=0)]^2 \rho(x) dx}{\int_{-\infty}^{\infty} \rho(x) dx}. \quad (19)$$

$\rho(x)$ represents the beam transverse distribution. For example, $\rho(x)$ may take the form of a Gaussian distribution, $e^{-\frac{x^2}{2\sigma_x^2}}$, where σ_x is the beam's RMS width, or a uniform distribution. The distribution function influences the extent to which the sextupole component contributes to emittance growth, as the field's non-linear components interact with the particle density profile in different ways depending on the distribution. The resulting normalized emittance induced by the sextupole field, for both Gaussian and uniform beam distributions, is given by:

$$\begin{aligned} \varepsilon_{n, \text{sextupole}} &= \frac{\sqrt{3}}{2} \sigma_x^3 \frac{e}{mc} L_{eff} \frac{\partial^2 B_y}{\partial x^2} \bigg|_{x,y=0}, \\ \varepsilon_{n, \text{sextupole}} &= \frac{1}{2} \sigma_x^3 \frac{e}{mc} L_{eff} \frac{\partial^2 B_y}{\partial x^2} \bigg|_{x,y=0}. \end{aligned} \quad (20)$$

From Eq. 20, the increasing transverse emittance from parasitic sextupole component is linear with the effective length of the sextupole component and cubically of the beam RMS

size. This indicates that larger beam sizes or stronger sextupole component can significantly increase emittance. To mitigate this effect, it may be necessary to insert a compensating sextupole lens near the solenoid. This compensator can counteract the sextupole component's influence by introducing an opposing sextupole field component. Additionally, reducing the second-order derivative of the transverse magnetic field in the solenoid can help diminish the sextupole component effect, as a smaller second-order derivative reduces the strength of the non-linear component that contribute to emittance growth.

III. NEW DESIGN OF THE SC SOLENOID

To reduce spherical aberration, we optimized the design of the SC solenoid. Magnetic field calculations were carried out using Poisson/Superfish, a software widely used for simulating electromagnetic fields in accelerator components [34]. The results of these calculations are displayed in Fig. 2. The NbTi wire coils remain unchanged in both designs, while the pure iron yoke was optimized by increasing its radius from $R_1 = 31.75$ mm to $R_2 = 38$ mm and doubling its length from $L_1 = 58.6$ mm to $L_2 = 120$ mm. This optimization significantly altered the solenoid's magnetic field profile. The normalized longitudinal field and its first derivative for both designs are shown in Fig. 3, where the new design displays a substantial reduction in the first derivative at the solenoid field's edges. The effective length of the solenoid increased from 40.56 mm to 52.27 mm in the new design.

We conducted simulations using ASTRA to compare the beam dynamics between the old and new solenoid designs. In these simulations, the beam kinetic energy was set to 3.5 MeV, and space charge effect was neglected to focus on the solenoid's impact on the beam. At the solenoid entrance, the beam had zero emittance with a Gaussian distribution transverse profile. The magnetic field integral B_z^2 was identical for both designs at $1.19 \times 10^{-3} \text{ T}^2 \cdot \text{m}$. The maximum magnetic fields were 0.171 T and 0.151 T for old-designed and new-designed, respectively. The integration of B_z first derivative square were $1.14 \text{ T}^2 \cdot \text{m}^{-1}$ for old-designed and $0.62 \text{ T}^2 \cdot \text{m}^{-1}$ for new-designed.

Fig. 4 presents the spherical aberration emittance at the solenoid exit for both designs. The new design demonstrated a marked improvement, with the fourth-power fitting coefficient being roughly half that of the old design. The coefficient is reduced about 47%, from $0.0061 \text{ mm}^{-3} \cdot \text{mrad}$ to $0.0033 \text{ mm}^{-3} \cdot \text{mrad}$. For a 600 pC beam with a Gaussian transverse distribution profile and 4.25 mm RMS size at solenoid position, the transverse projected emittance at 2.62 m far from the cathode decreases from $5.458 \text{ mm} \cdot \text{mrad}$ with old designing SC solenoid to $4.768 \text{ mm} \cdot \text{mrad}$ with new designing SC solenoid at the same focal strength. Additionally, when the solenoid is not aligned perfectly, new designing SC solenoid will behaviour much better. For instance, if the alignment has 1 mm offset in x-direction, the transverse projected emittance will decrease from $5.814 \text{ mm} \cdot \text{mrad}$ to $4.902 \text{ mm} \cdot \text{mrad}$. The average slice emittance decreases about 25%.

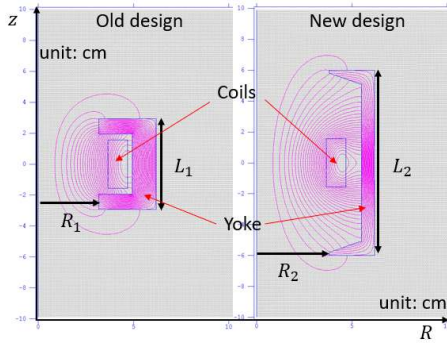


Fig. 2. The magnetic field simulation in Posion Superfish of the SC solenoid with old and new designs.

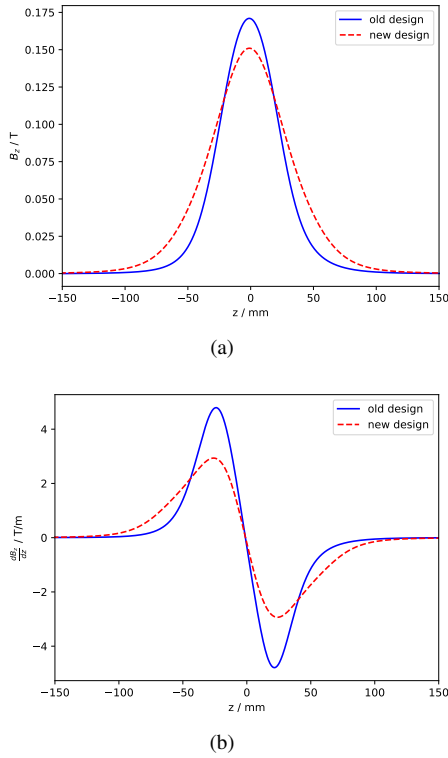


Fig. 3. The comparison between the normalized longitudinal magnetic field (a) and its first derivative (b) for the new and old SC solenoid designs at the same magnetic field integration

IV. MEASUREMENT SETUP

The multipole components arise when there is an offset or tilt between the solenoid's magnetic field axis and its mechanical axis. Misalignments of this kind can cause multipole components, such as quadrupole or sextupole, to appear. These multipole components distort the beam profile and increase transverse emittance, degrading overall beam quality. Identifying and correcting these misalignments is crucial for optimizing solenoid performance.

Fig. 5 presents a photograph of the magnetic field measurement system. The 3-D coordinate measurements and mechan-

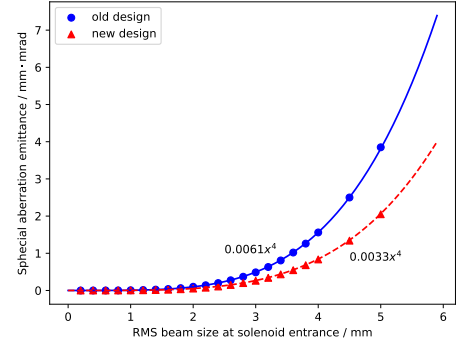


Fig. 4. Spherical aberrations effect.

ical alignment of the solenoid were performed using a Quantum Max metrology tool (mechanical measuring arm) from FARO. this arm was also employed to establish the transverse coordinate origin and ensure proper alignment of the longitudinal axis. Before sealing the cryomodule, this tool was used to determine the module's mechanical axis and the solenoid's position relative to the cryomodule's large front-side flange, which served as the reference plane.

The mapping of the magnetic field is carried out using three motorized linear stages enabling precise 3-axis movements. The z direction stage had a travel range from 0 to 270 mm. Fig. 6 shows the installation of SC solenoid in the cryomodule. The core fixed by the aluminium support frame is placed at 135 mm far from the measurement original point. The diameter of beam pipe is 39 mm. The z direction stage had a travel range from 0 to 270 mm.

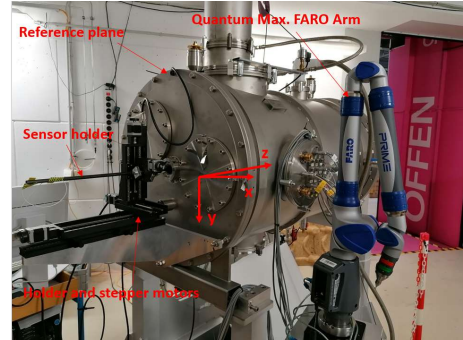


Fig. 5. Superconducting solenoid measurement system.

Magnetic field measurements are performed using two Hall sensors. The first sensor from SENIS AG is employed to measure all three components of the magnetic field. It operates within a range from - 200 to 200 mT, and the resolution is 0.001 mT. The active area of this 3-D probe measures $150 \mu\text{m} \times 150 \mu\text{m}$ with a thickness of $50 \mu\text{m}$. To ensure precise alignment and protection of the probes during the field mapping, a custom holder was designed (see Fig. 8 (a)). The second is a Magnet-Physik GmbH probe measuring the longitudinal magnetic field component with range from 3 mT to 3 T (see Fig. 8 (b)).

For the 1-D axial probe, measurements of the longitudinal

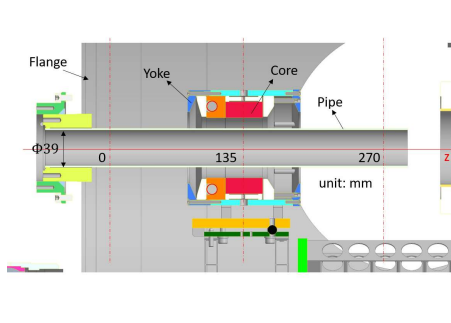
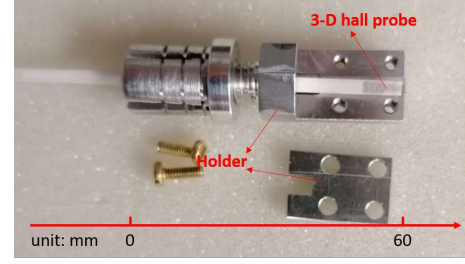
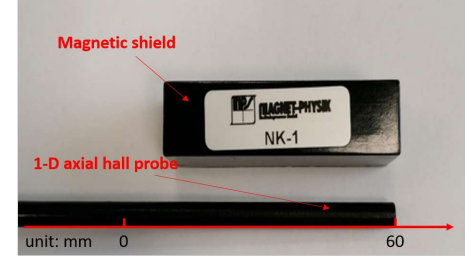


Fig. 6. The setup of cryomodule with SC solenoid, tube, and coordinate system.



(a)



(b)

Fig. 8. (a) 3-D hall sensor; (b) 1-D hall sensor.

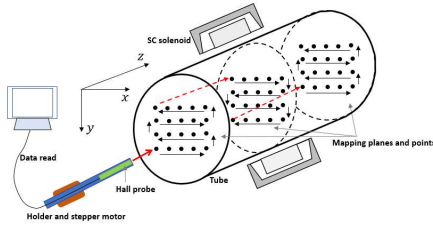
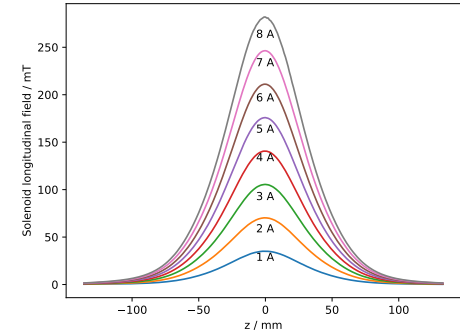


Fig. 7. The SC solenoid field mapping.

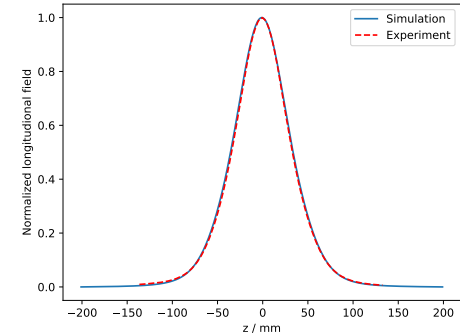
V. FIELD MEASUREMENT RESULTS

The longitudinal field B_z along the solenoid axis is measured using the 1-D Hall probe, which is selected for its ease of data processing, allowing for more efficient and accurate analysis compared to other methods. Due to the dominance of the longitudinal field over the weaker transverse components, any minor misalignment between the measurement and solenoid axes was considered negligible.

In Fig. 9 (a), the measured longitudinal field profile B_z is shown for currents ranging from 1 A to 8 A. Fig. 9 (b) compares this measured data with the computed field profile, revealing excellent agreement between the two. As anticipated from the solenoid's behavior, the maximum value of B_z exhibits a linear increase with the solenoid current, and the slope coefficient is 35.23 ± 0.02 mT/A, as Fig. 10 (a) illustrated. The effective magnetic length was determined to be 50.990 mm with a measurement uncertainty of ± 0.068 mm. The results for different currents, demonstrating the consistent relationship between field strength and current, are shown in Fig. 10 (b).



(a)



(b)

Fig. 9. The longitudinal field on axis of SC solenoid.

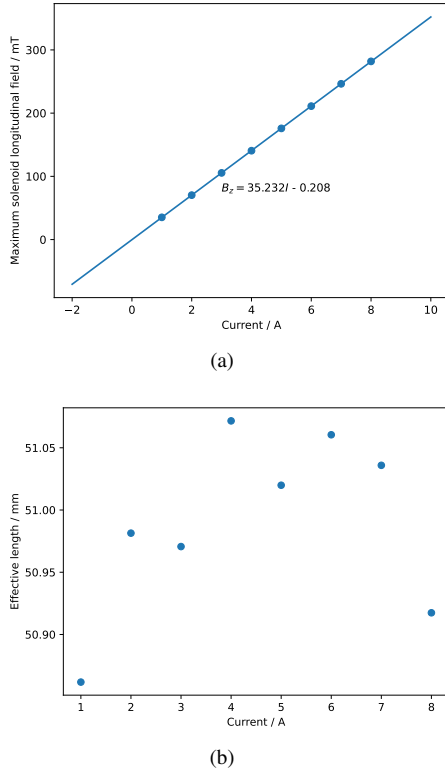


Fig. 10. The maximum longitudinal field on axis and effective length vs current.

A. Misalignment measurement

A detailed spatial field distribution mapping was performed to accurately measure the SC solenoid field, as depicted in Fig. 7. The 3-D Hall probe was used for these measurements, with the maximum current limited to 5 A due to the probe's range constraints. To account for the influence of background magnetic fields, a preliminary mapping was conducted at 0 A current. These background readings were subsequently subtracted from the standard field measurements before initiating numerical analysis.

The data analysis involved determining the extrema coordinates (maximum values outside and minimum values inside the solenoid) for each measurement plane using a parabolic fitting method. Linear regression method was applied to the center point coordinates in z direction at both the solenoid's entrance and exit, yielding two straight lines. The tilt and offset of the solenoid's field axis were calculated by averaging the results of these two lines. The SC solenoid offset is 2.27 ± 0.20 mm in horizontal and -0.51 ± 0.02 mm. The tilt is 7.86 ± 0.87 mrad in horizontal plane and -23.07 ± 1.23 mrad in vertical plane.

While the solenoid's offset can be adjusted by repositioning the x-y stage during SRF gun operation, any tilt in the solenoid's field axis, once established, cannot be corrected later. Potential sources of misalignment between the solenoid's magnetic field axis and the measurement axis include discrepancies between the solenoid's magnetic field

axis and the mechanical axis, inaccuracies in the solenoid's alignment relative to the reference plane, errors in the measurement coordinate system, and data analysis inaccuracies. Furthermore, magnetic hysteresis in the solenoid or adjacent components, as well as thermal contraction effects during the cooldown to 4.5 K, may also contribute to alignment deviations.

B. Multipole modes

The multipole components analysis focuses on the transverse magnetic field, measured using the 3-D Hall probe, to accurately characterize the higher-order magnetic field structures. Before performing the detailed evaluation of the field mapping data, background magnetic field measurements are subtracted to remove any residual environmental noise or baseline offsets, ensuring the accuracy of the subsequent analysis.

The main objective of the data processing is to compute the coefficients of the multipole modes, which describe the strength and nature of the magnetic field's higher-order components. These coefficients are calculated based on the measured transverse fields for each plane, following the formulation given in Eq. 7. Accurate center coordinates, which are essential for determining the symmetry and alignment of the multipole modes, are obtained from the previous axis measurements.

In the final step, a fitting procedure is applied to the data for each measurement plane, allowing for the extraction of the multipole coefficients that characterize the field's transverse components. As an illustrative example, Fig. 11 presents the multipole components distribution of the SC solenoid at 5 A. In Fig. 11 (a), the solenoid radial field coefficient J_t obtained from the measurement is compared with the corresponding curve derived from the first derivative of the measured B_z on axis. The good consistent between these two results confirms the validity and accuracy of the measurement process.

Fig. 11 (b) illustrates two components of the dipole field parasite in the solenoid. The normal mode exhibits symmetry around the solenoid's center, while the skew mode is asymmetric, indicating the presence of minor field imperfections.

The overall dipole field, accounting for both normal and skew modes, can be described by the following equation, which characterizes the field's complete dipole structure:

$$\mathbf{B}_d = \mathbf{B}_{dn} + \mathbf{B}_{ds} = -J_{ds}\mathbf{e}_x + J_{dn}\mathbf{e}_y \quad (21)$$

By integrating the transverse field components along the z axis, the resulting values determine the magnitude and direction of the dipole kick exerted on the beam. This kick influences the trajectory of the beam as it passes through the solenoid, with both strength and orientation depending on the transverse field distribution.

In Fig. 12 (a), the magnitude and phase of the dipole field are shown as a function of the longitudinal position z. Notably, a distinct phase change is observed at the central plane

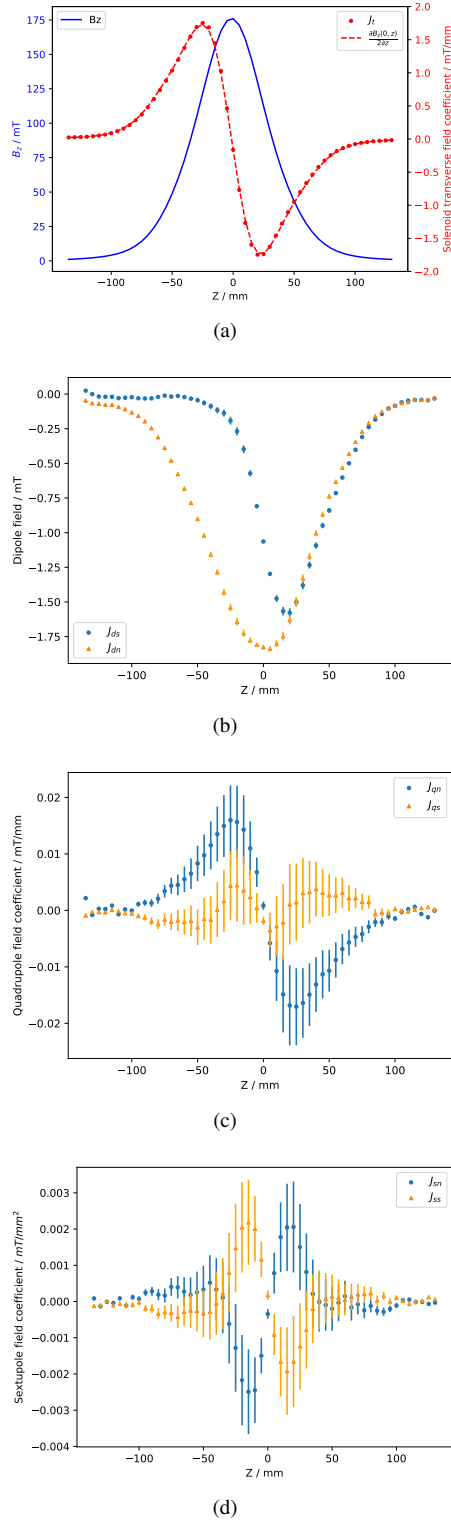


Fig. 11. SC solenoid transverse field multipole coefficients. (a) Solenoid radial field distribution; (b) Normal and skew dipole components distribution; (c) Normal and skew quadrupole components distribution; (d) Normal and skew sextupole components distribution.

in field symmetry across the solenoid.

As shown in Fig. 12 (b), the integration of dipole field strength is proportional with the current, confirming the proportional relationship between current and the transverse dipole field. This linearity is key for predicting the beam steering effects caused by the solenoid under varying operational conditions.

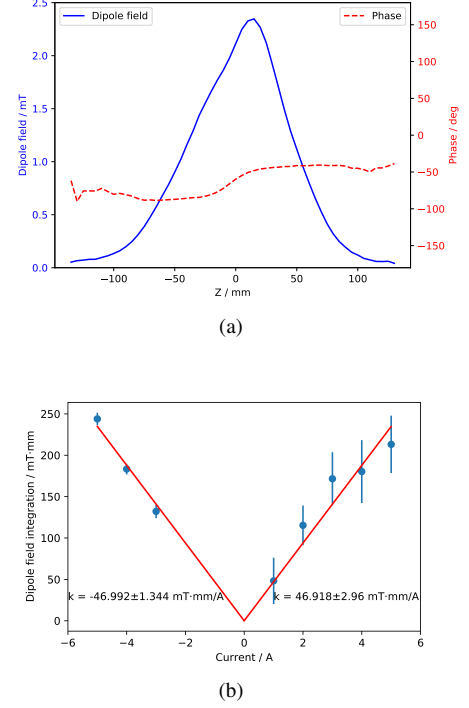


Fig. 12. (a) Dipole mode amplitude and phase distribution @ 5 A; (b) Integration of dipole mode strength vs solenoid current.

The parasitic quadrupole component, displayed in Fig. 11 (c), demonstrates antisymmetry about the solenoid's central plane, with the dominant normal quadrupole mode reversing its sign across the center. Due to this antisymmetry, the integrated quadrupole gradient, derived from the z -integration of the quadrupole components, is nearly zero. This suggests that, in the absence of other effects, the net focusing or defocusing from the quadrupole field is minimal over the entire solenoid.

However, the Larmor rotation of the beam's coordinate frame as it traverses the solenoid can cause a coupling between the transverse motions. This rotation may lead to observable effects on the beam, even when the integrated quadrupole field appears negligible. To accurately evaluate the total quadrupole field's impact on the beam, both the normal and skew components must be combined, as represented by the following equation:

$$\mathbf{B}_q = \mathbf{B}_{qn} + \mathbf{B}_{qs} = (J_{qn}y - J_{qs}x)\mathbf{e}_x + (J_{qn}x + J_{qs}y)\mathbf{e}_y \quad (22)$$

Fig. 13 (a) presents the polar representation of the quadrupole gradient, displaying both its magnitude and phase

with the longitudinal position z . This representation provides insight into the spatial variation and orientation of the quadrupole field components.

In Fig. 13 (b), the integrated quadrupole gradient is plotted with the solenoid current, revealing the linear dependence of the field strength on current. It is notable that the slopes for currents with different signs in Fig. 13 (b) differ slightly. This discrepancy may be attributed to systematic measurement errors, such as probe misalignment, noise in the data acquisition system, or non-ideal calibration of the Hall probes.

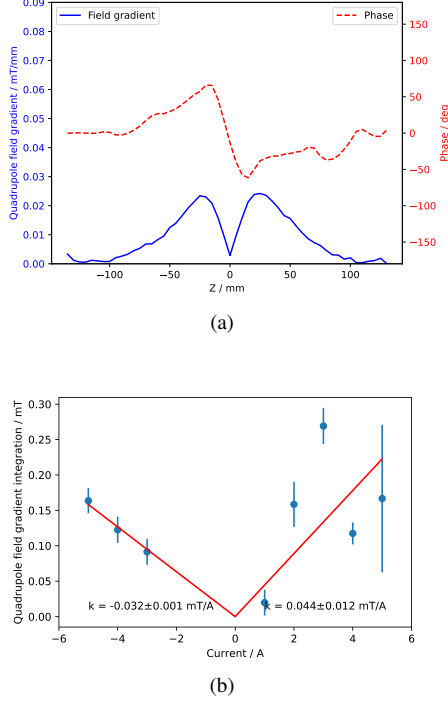


Fig. 13. Quadrupole field gradient and phase distribution @ 5 A (a); Integrated quadrupole gradient with current (b).

To mitigate the effects of the parasitic quadrupole field generated by the SC solenoid, a set of correctors, comprising one normal quadrupole and one skew quadrupole, is strategically placed 437 mm downstream from the solenoid center in the SRF gun beamline. Each corrector has an effective length of 0.0672 m and provides a gradient of 12 mT/m/A.

When operating SRF gun III at an accelerating gradient of 12 MV/m, corresponding to a kinetic energy of 6 MeV, the SC solenoid current is set to 6 A to focus the beam and mitigate the growth of transverse emittance. As a result, the solenoid induces an integrated quadrupole field gradient of 0.192 mT, with a peak value of 48 mT/m over an effective length of 4 mm.

Due to the uncertainty in the phase of the parasitic quadrupole field, simulations using ASTRA were conducted to analyze its impact on beam dynamics. Interestingly, under specific phase conditions, the parasitic quadrupole field can reduce the initial beam emittance, potentially compensating for the solenoid's spherical aberration. However, this effect is contingent on precise phase alignment.

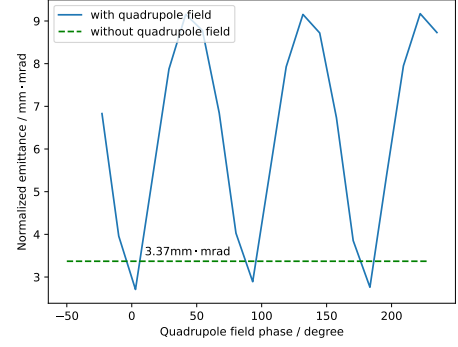


Fig. 14. Normalized emittance change with quadrupole field rotation angle in simulation. The beam with 500 pC bunch charge is 6 MeV of kinetic energy. We ignored the space charge when considered the quadrupole field in the solenoid. The solenoid current is 6 A located 55 mm downstream of the cathode. The component focal strength of parasitic quadrupole is 2.21 m^{-2} , and its effective length is 4 mm.

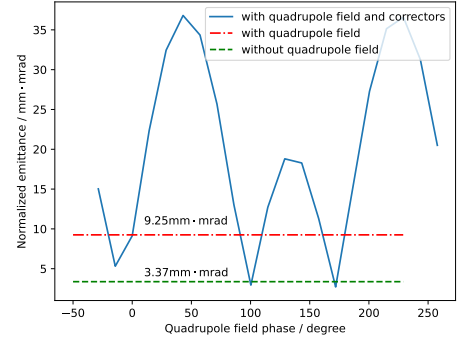


Fig. 15. Normalized emittance vs correctors rotation angle.

In most cases, the parasitic quadrupole field exacerbates transverse emittance growth, making it critical to cancel this effect using correction techniques. Assuming a worst-case scenario where the quadrupole field phase is misaligned by 45.8 degrees, as shown in Fig. 14, and applying a 1 A current to the corrector, Fig. 15 demonstrates that the emittance oscillation is significantly reduced. Simulation results confirm that the correctors, when properly adjusted, effectively nullify the influence of the solenoid's parasitic quadrupole field, thus preventing additional emittance growth.

$$\mathbf{B}_s = \mathbf{B}_{sn} + \mathbf{B}_{ss} = [J_{sn}xy - \frac{1}{2}J_{ss}(x^2 - y^2)]\mathbf{e}_x + [\frac{1}{2}J_{sn}(x^2 - y^2) + J_{ss}xy]\mathbf{e}_y. \quad (23)$$

The sextupole field characteristics are illustrated in Fig. 16 (a), which shows the sextupole field coefficient and its phase along the longitudinal direction at a solenoid current of 5 A. The amplitude of the sextupole field is approximately symmetric with respect to the original point (the solenoid's center), with maximum values of around 0.0025 mT/mm^2 occurring at the mirror planes. Additionally, the phase undergoes significant changes near the center, with maximum and

minimum strength values observed at these mirror planes. At the edges of the solenoid, the phase measurement becomes unstable due to the small magnitude of the sextupole coefficient, which results in significant noise interference and limits accurate fitting. Although it is expected that the z-integral of the sextupole field coefficient should be proportional to the solenoid current, the measured results do not align with this expectation, as shown in Fig. 16 (b). This discrepancy likely arises because the sextupole component falls outside the measurement method's accuracy range.

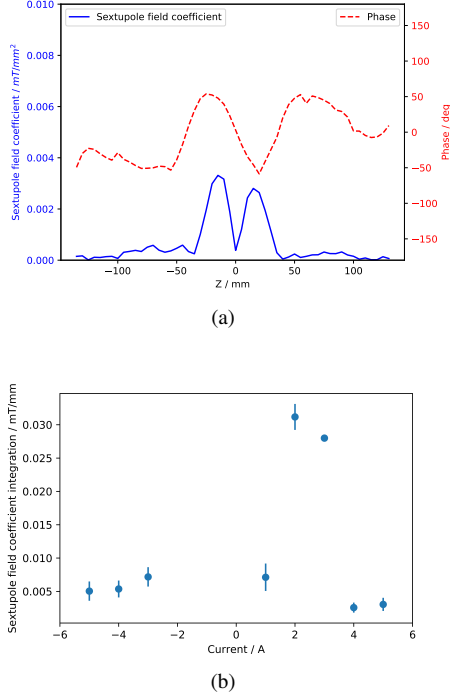


Fig. 16. (a) Sextupole field coefficient and phase distribution @ 5 A; (b) Integration of sextupole field coefficient vs solenoid current.

We evaluate the influence of the sextupole field on transverse emittance in the context of SRF gun III, utilizing a bunch charge of 500 pC. Simulations reveal that the beam's RMS size at the solenoid position is approximately 4 mm. With the solenoid current fixed at 6 A, the sextupole field exhibits an amplitude of approximately 0.005 mT/mm², with an effective length of 6 mm. For a beam characterized by a lateral Gaussian distribution of transverse profile, the additional normalized emittance introduced by the sextupole field is approximately 0.9 mm-mrad. In contrast, for a uniform beam distribution, the additional emittance is reduced to about 0.52 mm-mrad. Consequently, based on Eq. 20, the overall impact of the sextupole field on the transverse emittance is estimated to be approximately 20 %.

C. The analysis of error sources

The measurement uncertainties associated with the SC solenoid stem from four primary sources: 1. Mechanical

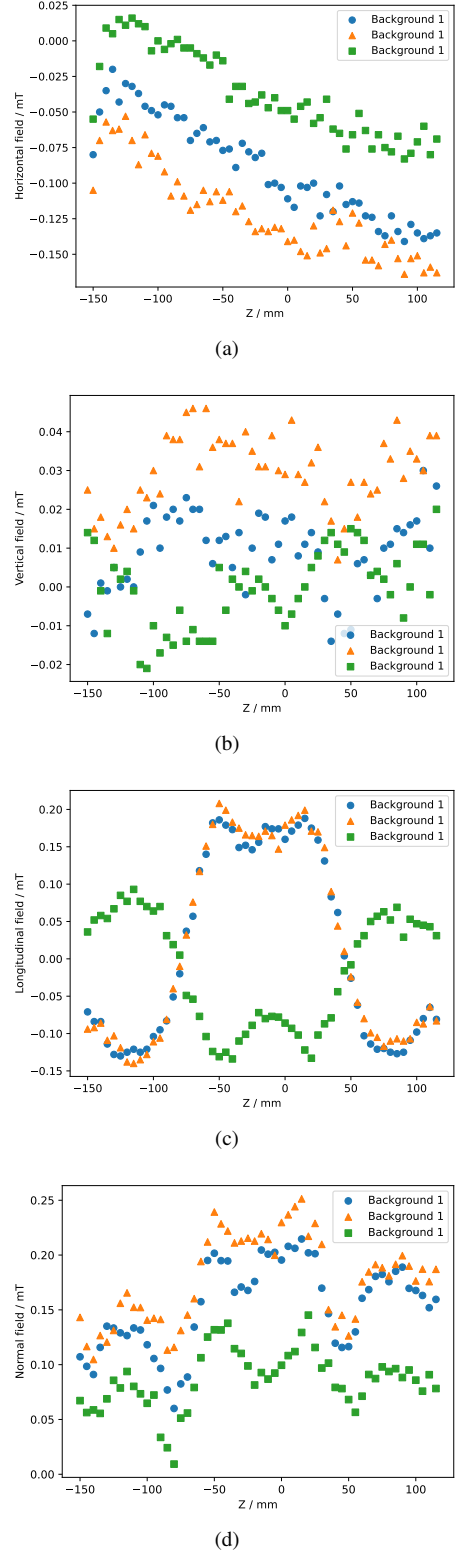


Fig. 17. Background field distribution.

Alignment of the Hall Probe: Inaccuracies in the mechanical alignment of the Hall probe can lead to erroneous measurements of the magnetic field. Even slight misalignments

may result in significant discrepancies in the recorded data. 2. Degaussing of the Yoke: Incomplete or imperfect degaussing of the yoke can introduce residual magnetic fields, which may affect the accuracy of the measurements by masking or distorting the intended signal. 3. Intrinsic Errors of the Hall Probe: Each Hall probe has inherent measurement errors due to its construction and operating principles, which can contribute to the overall uncertainty in the magnetic field measurements. 4. Data Fitting Errors: Errors introduced during the data fitting process can arise from the mathematical models used, as well as the selection of fitting parameters. These can affect the accuracy of the derived magnetic field values.

The field measurements were conducted over the course of one week, with each full mapping session taking approximately four and a half hours. Due to limitations in the measurement system—such as the z-axis movement range and the initialization procedure—the Hall probe required manual realignment with a marker on a daily basis. This manual realignment resulted in a longitudinal position error of less than 0.8 mm and a rotational error of less than 60 mrad. Consequently, the longitudinal field error of the solenoid due to realignment is estimated to be less than 2%, while the uncertainty in the transverse field is less than 6%.

The second source of error arises from the incomplete degaussing of the soft iron yoke. While a background field was recorded, it was not measured before each individual mapping session. Background measurements were taken at three key instances: initially before the measurement period, just prior to increasing the solenoid current to 4 A and then to 5 A, and finally after measuring the magnetic field at -3 A. As illustrated in Fig. 17, the background field's variation on the mechanical axis is approximately 0.125 mT. Although we subtracted this background field before performing the multipole field analysis, its variations introduce additional uncertainties. The averaged differences in the multipole component integrals are approximately 18.4% for dipole fields, 30.4% for quadrupole field gradients, and 21.4% for sextupole field coefficients.

Regarding the measurement equipment, the active area of the 1-D hall sensor is circle area with a diameter of 0.4 mm, representing an average over a circular area of 0.126 mm². The calibration uncertainty for the 1-D hall probe is 0.25% [36]. For the 3-D Hall sensor, the core size is 0.15 mm × 0.1 mm × 0.15 mm, and the measuring precision is better than ±0.1% [37]. Additionally, the intrinsic alignment error of the sensor areas in the 3-D Hall sensor is approximately 17.45 mrad, as shown in Fig. 18 [37].

Fig. 11 illustrates that the fitting errors are predominantly associated with the quadrupole field gradient and sextupole field coefficients. In contrast, the average fitting error in simulations, attributed to finite grid size, is less than 1%. The observed fitting errors are 2%, 73%, and 90% for the dipole field, the quadrupole field gradient, and the sextupole field coefficients, respectively.

The overall fitting error is a reflection of the cumulative impact of these individual errors, underscoring the significant

influence that the quadrupole and sextupole components have on the accuracy of the multipole field measurements. This

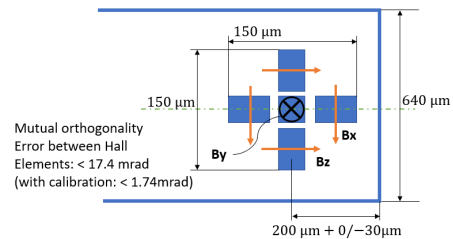


Fig. 18. 3-D sensor inside alignment.

highlights the importance of addressing these fitting errors to improve the reliability of the measurements.

VI. CONCLUSION

We have optimized the SC solenoid design to reduce spherical aberration, focusing on modifying the geometry and field distribution. The effective length and field strength coefficient, as determined from measurements under operational current, were found to be in excellent agreement with simulation results, confirming the accuracy of our solenoid design.

An analysis of the high-order magnetic components, including quadrupole and sextupole components, was conducted to assess their impact on beam transverse emittance. While the formalism fitting method used for multipole components analysis does not yield highly precise results due to the reasons discussed in the previous section, it provides valuable insights into the solenoid's performance in the beamline and helps guide further optimization efforts.

The correctors installed in the beamline effectively compensate for the adverse impact of the quadrupole field on beam transverse emittance. However, the sextupole component remains a critical factor in optimizing the injector's future performance, as it introduces non-linear field effects that significantly impact beam quality.

To mitigate the effects of the sextupole component, a practical solution is to install a sextupole corrector in close proximity to the SC solenoid. This would allow for fine-tuning of the higher-order field components and enhance the overall beam quality. This addition could significantly enhance performance by further mitigating the sextupole effects, optimizing the injector's performance.

VII. ACKNOWLEDGEMENTS

Thanks to the helpful discussion with Dr. Houjun Qian from Zhang Jiang Lab, Chinese Academy of Science.

VIII. REFERENCES

- [1] F. Gabriel, P. Gippner, E. Grosse et al., The Rossendorf radiation source ELBE and its FEL projects. *Nucl. Instrum. Methods Phys. Res., Sect. A* **161**, 1143-1147 (2000).
- [2] P. Michel, ELBE center for high-power radiation sources. *J. Large-Scale Res. Facil.* **2**, A39 (2016).
- [3] M. Helm, S. Winnerl, A. Pashkin et al., The elbe infrared and thz facility at helmholtz-zentrum dresden-rossendorf, *Eur. Phys. J. Plus*, **138**, 158 (2023).
- [4] A. Arnold, J. Teichert, Overview on superconducting photoinjectors, *Phys. Rev. Accel. Beams* **14**, 024801 (2011).
- [5] J. Teichert, A. Arnold, G. Ciovati et al, Successful user operation of a superconducting radio-frequency photoelectron gun with Mg cathodes, *Phys. Rev. Accel. Beams* **24**, 033401 (2021).
- [6] J. Teichert, A. Arnold, H. Büttig et al., Free-electron laser operation with a superconducting radio-frequency photoinjector at ELBE, *Nucl. Instrum. Methods Phys. Res., Sect. A* **743**, 114 (2014).
- [7] R. Xiang, A. Arnold, J.W. Lewellen, Superconducting radio frequency photoinjectors for CW-XFEL, *AIP CONF. PROC.*, **11**, 1166179 (2023).
- [8] R. Xiang, A. Arnold, P. Lu et al, Study of magnisium photocathodes for superconducting rf photoinjectors, in *Proceedings of the 2018 International Particle Accelerator Conference*, Vancouver, Canada (JACoW, Geneva, 2018), p. 4142.
- [9] J. Schaber, R. Xiang, W. Gaponik, Review of photocathodes for electron beam sources in particle accelerators, *J. Mater. Chem. C*, **11**, 3162-3179 (2023)
- [10] P. Lu, Optimization of an SRF gun for high bunch charge applications at ELBE, Ph.D. thesis, TU Dresden, 2017.
- [11] J. Klug, E. Altstadt, C. Beckert et al., Development of a neutron time-of-flight source at the ELBE accelerator, *Nucl. Instrum. Methods Phys. Res., Sect. A* **577**, 641 (2007).
- [12] X. J. Wang, P. Musumeci, Report of the Basic Energy Sciences Workshop on the Future of Electron Sources, SLAC National Accelerator Laboratory, 2016.
- [13] B. Green, S. Kovalev, V. Asgekar et al., High-field high-repetition-rate sources for the coherent THz control of matter, *Sci. Rep.* **6**, 22256 (2016).
- [14] A. Jochmann, A. Irman, M. Bussmann et al., High Resolution Energy-Angle Correlation Measurement of Hard X Rays from Laser- Thomson Backscattering, *Phys. Rev. Lett.* **111**, 114803 (2013).
- [15] H. Vennekate, A. Arnold, P. Lu et al., Emittance compensation schemes for a superconducting rf injector, *Phys. Rev. Accel. Beams* **21**, 093403 (2018).
- [16] H. Vennekate, Emittance Compensation for SRF Photoinjectors, Ph.D. thesis, TU Dresden, 2017.
- [17] M.E. Schulze, Spherical Aberrations-Final Focus and Solenoid Scans, Los Alamos National Lab (LANL), Los Alamos, NM (United States) (2020).
- [18] D. H. Dowell, Sources of Emittance in RF Photocathode Injectors: Intrinsic emittance, space charge forces due to non-uniformities, RF and solenoid effects, *arXiv preprint arXiv:1610.01242* (2016).
- [19] S. Ma, A. Arnold, P. Michel et al., The application of encoder-decoder neural networks in high accuracy and efficiency slit-scan emittance measurements, *Nucl. Instrum. Methods Phys. Res., Sect. A* **1050**, 168125 (2023).
- [20] L. M. Zheng, J. H. Shao, Y. C. Du et al., Experimental demonstration of the correction of coupled transverse dynamics aberration in an rf photoinjector, *Phys. Rev. Accel. Beams* **22**, 072825 (2019).
- [21] E. Prat, P. Dijkstal, M. Aiba et al., Generation and characterization of intense ultralow-emittance electron beams for compact x-ray free-electron lasers, *Phys. Rev. Lett.* **123**, 234801 (2019).
- [22] M. Altarelli, The European X-ray free-electron laser facility in Hamburg, *Nucl. Instrum. Methods Phys. Res., Sect. B* **269**, 2845-2849 (2021).
- [23] E. A. Seddon, J. A. Clarke, D. J. Dunning et al., Short-wavelength free-electron laser sources and science: a review, *Rep. Prog. Phys.* **80**, 115901 (2017).
- [24] H. Vennekate, A. Arnold, P. Lu et al., Building the Third SRF Gun at HZDR, RF and solenoid effects, In *Proceedings of the 2017 International Beam Instrumentation Conference (IBIC'17)*, Geneva, Switzerland(JACoW, Geneva, 2017), p. 98
- [25] K. Zhou, A. Arnold, P. Li et al., Preliminary Geometry Optimization of a 3.5-Cell SRF Gun Cavity at ELBE Based on Beam Dynamics, In *Proceedings of the 2019 Free Electron Laser Conference (FEL'19)*, Hamburg, Germany(JACoW, Geneva, 2019), p. 374
- [26] D. Arbelaez, A. Madur, L. M. Lipton et al., Magnetic alignment of pulsed solenoids using the pulsed wire method. in *Proceedings of the 2011 International Particle Accelerator Conference*, New York, USA (JACoW, Geneva, 2011), p. 2087-2089.
- [27] P. Arpaia, M. Buzio, J. J. G. Perez et al., Magnetic field measurements on small magnets by vibrating wire systems, 2011 IEEE International Instrumentation and Measurement Technology Conference, IEEE, 1-4 (2011).
- [28] P. Arpaia, C. Petrone, S. Russenschuck et al., Vibrating-wire measurement method for centering and alignment of solenoids, *J. INSTRUM.*, **8**, P11006 (2013).
- [29] H. Wiedemann, *Particle accelerator physics*, Springer Nature (2015).
- [30] D. H. Dowell, F. Zhou, J. Schmerge, Exact cancellation of emittance growth due to coupled transverse dynamics in solenoids and RF couplers. *Phys. Rev. Accel. Beams*, **21**(1):010101, 2018.
- [31] K. Flöttmann, ASTRA: A space charge tracking algorithm, manual, version 3, 2011, update April 2014.
- [32] Q. Jiang, S. D. Anderson, D. Dowell et al., Beam Dynamics Simulation of the Solenoid Sextupole Error in the LCLS-II Injector, SLAC National Accelerator Lab., Menlo Park, CA (United States) (2018).
- [33] D. H. Dowell, Correcting emittance growth due to stray sextupole fields, *arXiv preprint arXiv:1810.00086*(2018).
- [34] J. H. Billen, L. M. Young, POISSON/SUPERFISH on PC compatibles. In *Proceedings of International Conference on Particle Accelerators*, Washington, DC, USA, vol. 2, 790-792 (1993).
- [35] J. Vanderlinde, *Classical electromagnetic theory*, Springer Science & Business Media (2006).
- [36] Magnet-Physik Dr. Steingroever GmbH. USB Hall probes. Köln (2008).
- [37] SENIS magnetic & current measurement. Fully integrated 3-Axis Hall Probe HL, HM, HS. SENIS AG, Switzerland (2017).
- [38] M. Reiser, *Theory and design of charged particle beams*, John Wiley & Sons (2008).